Vacuum-Deposited Multication Tin-Lead Perovskite Solar Cells

Ana M. Igual-Muñoz,[1] Aroa Castillo,[1] Chris Dreessen,[1] Pablo P. Boix,*[2] and Henk J. Bolink.*[1]

[1] Instituto de Ciencia Molecular, Universidad de Valencia, C/ J. Beltran 2, 46980 Paterna, Spain.

[2] Institut de Ciència dels Materials, Universitat de València, C/ J. Beltran 2, 46980 Paterna, Spain.

*E-mail: Pablo.P.Boix@uv.es; henk.bolink@uv.es

ABSTRACT

The use of a combination of tin and lead is the most promising approach to fabricate narrow bandgap metal halide perovskites. This work presents the development of reproducible tin and lead perovskites by vacuum co-deposition of the precursors, a solvent-free technique which can be easily implemented to form complex stacks. Crystallographic and optical characterization reveal the optimal film composition based on cesium and methylammonium monovalent cations. Device optimization makes use of the intrinsically additive nature of vacuum deposition, resulting in solar cells with 8.89% photovoltaic efficiency. The study of the devices by impedance spectroscopy identifies bulk recombination as one of the performance limiting factors.

KEYWORDS: Perovskite, Low-bandgap, Tin-lead, Solar cell, Vacuum-deposition

INTRODUCTION

The efficiency of metal halide perovskite solar cells has increased from 2.2% in 2006 up to 25.2% in 2019.[1–3] The best results to date are based on perovskite employing lead (Pb) and a combination of multiple monovalent cations and halides, with a bandgap between 1.5 and 1.6 eV.[4] A number of approaches

can be adopted to further increase the perovskite solar cells power conversion efficiency, most of which require adjusting the absorber's bandgap. For example, targeting single junction cells with efficiency close to the Shockley-Queisser limit (ideal bandgap of ~1.34 eV),[5] or exploiting the full potential of multi-junction solar cells with current-matching absorbers.[6]

The substitution of Pb by tin (Sn) in this family of materials leads to an absorption bandgap narrowing, with values down to 1.1 eV.[7-8] Nevertheless, the use and manufacturing of pure tin-based perovskites is not trivial due the easy oxidation of Sn^{2+} to Sn^{4+} which leads to p-type doping and compromises the device stability and performance.[9] Partial Pb substitution is an alternative route which increases the flexibility of the approach, widening the number of possible compositions. Indeed, perovskites combining both metals can form narrower bandgap materials as the values are not linear with the metals ratio,[10] particularly useful for the fabrication of perovskite-perovskite tandems.[11] More interestingly, mixed tin and lead compositions present enhanced stability compared to pure Sn-based ones, as the introduction of Pb into the perovskite retards the oxidation from Sn^{2+} to Sn^{4+},[12] analogously to the introduction of germanium in the structures which forms a native-oxide layer on the perovskite.[13] Recent studies have achieved efficiencies as high as 20.5% with devices employing tin-lead based perovskites.[14–16] The fabrication of these devices employ a solution-based process with important restrictions on the thickness control and solvent compatibility, which limit their direct application to multijunction devices. Among all the alternative methods for the perovskite synthesis, physical vapor co-deposition of the precursors presents several advantages that make it particularly interesting for the industrialization of the field.[17] This technique is intrinsically additive and solvent-free which allows for an accurate control on the film thickness and multi-stack formation versatility, key points for the fabrication of multi-junction tandem devices.[18] Vacuum deposition is also compatible with large area film formation, enabling the control over the morphology and thickness of the film. In addition to these advantages, the technique has led to high efficiency photovoltaic devices with different Pb-based perovskite compositions.[19-20] We recently reported efficient vacuum-deposited formamidinium tin-lead based perovskite solar cells.[21] However, these studies rely on the use of SnF_2 to reduce the formation of Sn^{4+} as a degradation byproduct;[9,22] and on the formamidinium as the sole monovalent cation in the final perovskite. Small quantities of reactants, such as those required for the SnF_2 in Sn-Pb perovskites, are less easy to control by co-evaporation, and the cristallization of pure formamidinium is associated to phase control difficulties. The combination of these factors results in low reproducibility and compromises the material stability, and the work serves primarily as a proof of concept of the capability to synthesize these perovskites by co-evaporation. The fabrication of tin-lead based perovskites combining cesium (Cs) and formamidinium (FA) as monovalent cations through dual source evaporation has also been reported.[23] This work pre-synthetized some of the precursors as an alloy, and still required the use of SnF_2.

Following that path, the incorporation of two monovalent cations is a promising approach to palliate the abovementioned drawbacks, as methylammonium (MA) and Cs based tin-lead perovskites have shown the capability to operate without SnF_2 additives.[24] In particular, introducing Cs can enhance the perovskite thermal stability, photostability and efficiency,[25-26] yet their use in Sn-Pb perovskites fabricated by precursor co-evaporation remains unexplored. In addition, MA is more stable and controllable than FA through evaporation methods. As a result, these vacuum-deposited perovskites are significantly more reproducible than those employing FA. [21]

In this work, we study the partial replacement of Pb^{2+} by Sn^{2+} in a $MA_{0.9}Cs_{0.1}PbI_3$ perovskite fabricated by simultaneous thermal vacuum deposition of the precursors, avoiding the use of SnF_2. The targeted composition was 25% Sn 75% Pb, following previous reports which showed that this composition leads to enhanced stability and higher efficiencies.[25] The obtained perovskite presents a lower energy absorption onset than its Pb-based counterpart, with a bandgap close to the optimal one for single junction solar cells (1.34 eV),[5] and suitable for future use as low-bandgap absorber in a tandem device. The film characteristics, such as morphology and crystallinity, are modified by adjusting the evaporation parameters. Evaluating different thicknesses of Sn-Pb perovskites in a multilayer solar cell results in devices with efficiency close to 9%.

EXPERIMENTAL SECTION

Synthesis of $MA_{0.9}Cs_{0.1}Sn_{0.25}Pb_{0.75}I_3$. The precursors used in this study were tin (II) iodide (SnI_2)(>97%), lead (II) iodide (PbI_2)(>98%), cesium iodide (CsI) (>99%) from Tokio Chemical Industries (TCI) and methylammonium iodide (MAI) (>99,5%) from Lumtec. The $MA_{0.9}Cs_{0.1}Sn_{0.25}Pb_{0.75}I_3$ films were fabricated by simultaneous thermal vacuum deposition of the precursors MAI, SnI_2, PbI_2 and CsI without further thermal treatment on the substrate. In order to stablish the proper deposition of the precursors, calibration of their thickness was done prior to the synthesis of the perovskite. This calibration factor was obtained by depositing an amount of each precursor on a glass substrate and measurement of its thickness with a mechanical profilometer. Furthermore, it should be indicated that the rates of evaporation depend on the reading capability of the Quartz crystal microbalances (Fil-Tech). This factor can slightly change during long evaporations due to material deposition on the microcrystal. The evaporation was done in a vacuum chamber at a pressure of 3×10^{-6} mbar. Four crucibles were filled with the different precursors and evaporated at the temperatures of 90 ºC for MAI, 176 ºC for SnI_2, 287 ºC for PbI_2 and 386 ºC for CsI. The thickness of the films was controlled by the sum of the rates of SnI_2 and PbI_2 being 0.2 and 0.59 Å s^{-1} each. Employing these rates, it takes between 1 and 3 hours to synthesize the perovskites, depending on the final

film thicknesses. A scheme of the evaporator may be found in Fig S1 to identify each precursor with the source that was employed for them.

Device preparation. Molybdenum oxide (MoO3) and bathocuproine (BCP) were obtained from Lumtec, 4,4′,4″-Tris[(3-methylphenyl)phenylamino]triphenylamine (m-MTDATA) and C_{60} were obtained from Sigma Aldrich. Inside a metal chamber at a pressure of $2x10^{-6}$ mbar, 5 nm of MoO_3 was thermally evaporated on indium tin oxide (ITO) patterned substrates and annealed at 100 ºC for 10 minutes. After this 10 nm of m-MTDATA was thermally evaporated at a pressure of $3x10^{-6}$ mbar. Then, the $MA_{0.9}Cs_{0.1}Sn_{0.25}Pb_{0.75}I_3$ films were fabricated following a similar procedure as described above. On top of the perovskite 25 nm of C_{60} and 8 nm films of BCP were evaporated at a pressure of $3x10^{-6}$ mbar. Finally, 100 nm of Ag was deposited at a pressure of $2x10^{-6}$ mbar. Resulting in completely sublimed devices. The samples were kept in inert atmosphere in between the deposition of the different materials.

Current-voltage characteristics. Solar cells were characterized by current voltage sweeps recorded with a Keithley Model 2400. The solar spectrum (AM1.5G) used for the illuminated curves was corrected with a calibrated silicon reference cell (Minisun simulator by ECN, Netherlands). IPCE measurements were done by applying different wavelengths employing band-pass filters on a white halogen lamp and measuring the response of the cell. A shadow mask with an aperture of $0.0264cm^2$ was employed to avoid illumination of non-active area.

Impedance spectroscopy. A Gamry Interface 1000 Potentiostat was used to apply a frequency variable (from 100 MHz to 0.1 Hz) AC voltages (20 mV amplitude) at different DC potentials (from open circuit to short circuit conditions) under one sun illumination. Z-View software was used to fit the results to an equivalent circuit.

Structural analysis. The crystalline structure of the perovskites was studied by grazing incident X-ray diffraction (GIXRD). The patterns were collected on an Empyrean PANalytical powder diffractometer using Cu Kα1 radiation. A scanning electron microscope (SEM) Hitachi S-4800 operating at 20 kV accelerating voltage was used to obtain SEM images. Samples were platinum-metallized prior to their observation. The microscope incorporated an X-Ray detector Broker and the program QUANTAX 400 for Energy Dispersive X-Ray Analysis (EDAX).

Optical analysis. UV-Vis absorption spectra were collected using a fiber optics Avantes Avaspec2048 Spectrometer. Tauc plot was calculated employing the formula $(\alpha h\upsilon)^2$.

RESULTS AND DISCUSSION

The monovalent to divalent metal cation ratio determines the ultimate optoelectronic properties of the resulting perovskite film. We targeted a composition ($MA_{0.9}Cs_{0.1}Sn_{0.25}Pb_{0.75}I_3$). To achieve this, films of different conditions were explored and evaluated off-line. This was done by modifying the precursor deposition rates. The PbI_2:SnI_2 and CsI:MAI ratios were maintained unaltered, and the parameter explored was the SnPb to MACs ratio (defined as the sum of the SnI_2 and PbI_2 deposition rates, and the sum of MAI and CsI deposition rates respectively).

In order to find the optimal deposition conditions, perovskite films with precursor ratios varying from 1.2:1 to 2.3:1 (SnPb:MACs) were analyzed by XRD (Fig. S2a) to understand possible crystallographic differences and by UV-Vis absorbance (Fig. S2b) to understand their optical properties. These films when integrated into a device were also used in preliminary solar cells to evaluate their photovoltaic performance (Fig. S3). In the XRD patterns in Fig. S2 a peak at 11.4º related to low dimensional perovskites can be observed. This suggests a lack of divalent cationic component in the 1.2:1 ratio because this feature appears when there is an excess of MA in the films.[27–29] The XRD pattern for the 2.03:1 ratio is the expected one, with all the peaks observed related to the formation of the targeted perovskite. The small excess of divalent cations has been reported to increase the device performance and circumvent the need of SnF_2.[30] For this purpose, a final ratio of 2.3:1 was investigated, which results in a peak related to excess of SnI_2/PbI_2 centered at 12.7º.

The absorbance analysis (Fig. S2a) of samples based on the 1.2:1 ratio shows the decay of absorption around 850 nm, corresponding to a not fully formed perovskite bandgap. In contrast, the ratios 2:1 and 2.3:1 result in the expected absorbance onset at 950 nm, with higher absorption in the whole spectrum for the 2.3:1 sample. Unoptimized solar cell performance for all the compositions is displayed in the supplementary information (Fig S3, Table S1). Based on the unoptimized solar cells performance and in concordance with previous studies indicating that the perovskite with a small excess of divalent cations has benefits ,[30] the perovskite based on the 2.3:1 ratio was chosen for the detailed study described in this

manuscript. A preliminary evaluation of thermal post-treatment effects, shown in Fig S4(a, b), indicates that the annealing in N_2 atmosphere does not result in a photovoltaic improvement, which confirms previous results on co-evaporated solar cells. Finally, a shelf-stability estimation of these cells. These cells were measured as prepared and after three days of storage in a glovebox, showing no significant changes in performance but a slight decrease in current and fill factor. This results are shown in Fig S5 (a,b).
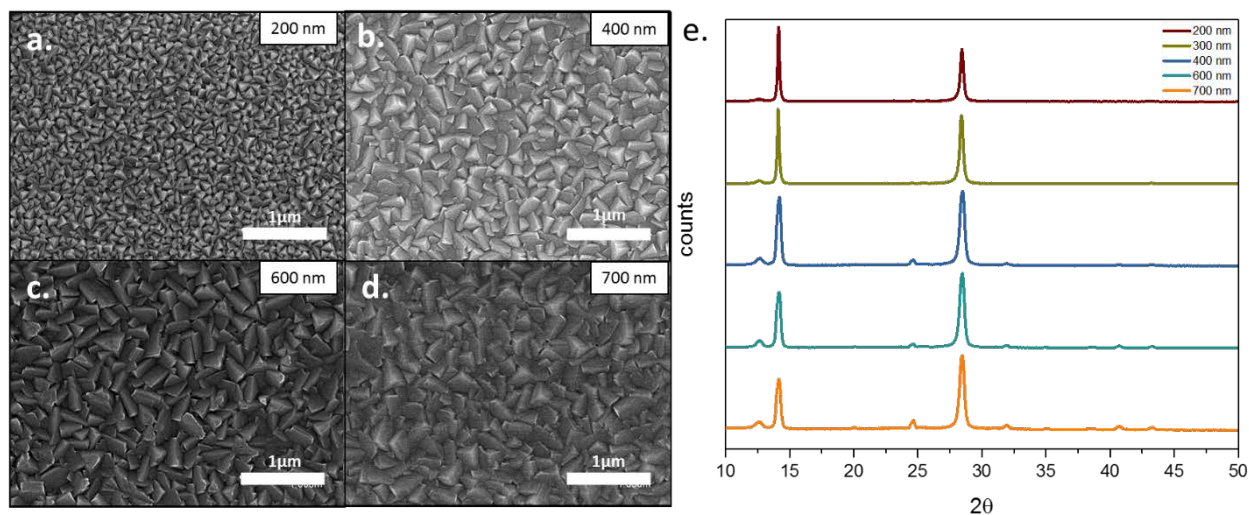
Fig. 1. (a-d) Top view SEM images of MA$_{0.9}$Cs$_{0.1}$Sn$_{0.25}$Pb$_{0.75}$I$_3$ films with different thicknesses. (e) XRD diagrams of MA$_{0.9}$Cs$_{0.1}$Sn$_{0.25}$Pb$_{0.75}$I$_3$ films with different thicknesses.

The thickness and quality of the films (morphology, crystallinity, and optoelectrical properties) are key parameters for incorporating a film as the absorber in a photovoltaic device. Fig. 1a-d shows the top view SEM images for perovskite films with different thicknesses. In general, the vacuum-based deposition process results in a pinhole-free film with well-defined crystals, which suggests that high quality crystalline perovskite films can be obtained. On the other hand, a slight increase of the grain size may be observed for thicker films. This was attributed to the slight decrease in MAI rate during the deposition, which is more pronounced for thicker samples as the procedure is longer. The previously discussed XRD pattern is reproduced for all the samples, corresponding to the typical pattern for Sn-Pb perovskites,[11,25] and an additional peak at 12.7 ° related to tin-lead excess (see Fig. 1e), which was shown to be beneficial for the solar cells performance in previous studies.[30] The XRD results display a trend related to the film thickness, with thicker films increasing the intensity in the plane (220). This, however, could be considered an artifact

of the measurement, as the incident beam at low angles only reaches the surface whereas at higher angles it reaches the whole sample. As a result, thicker samples present more intense higher angles peaks.

To determine the bandgap of the films in detail, UV-Vis absorbance results of the films where analyzed (Fig. 2a), with a Tauc plot, plotted as $(\alpha h\upsilon)^2$ vs energy(eV), (inset of Fig. 2a). As expected, an increase in the absorbance is concomitant to the increase in the film thickness while the bandgap is maintained.
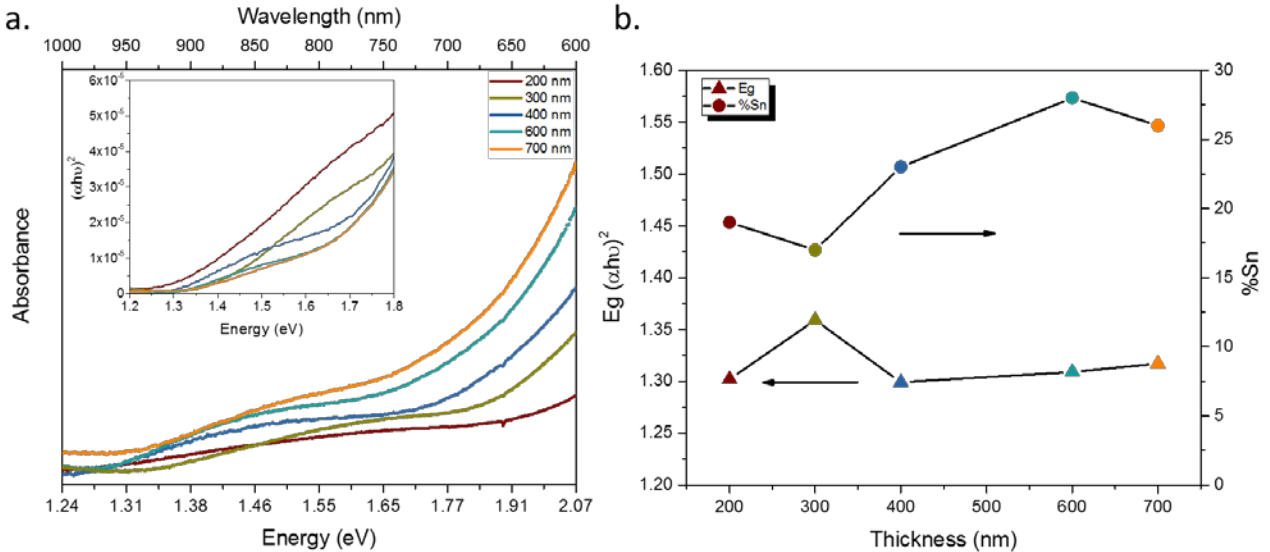
Fig. 2. (a) UV-Vis Absorbance for MA$_{0.9}$Cs$_{0.1}$Sn$_{0.25}$Pb$_{0.75}$I$_3$ films with different thicknesses. Inset: Tauc plot of the absorbance data. (b) Bandgap obtained from the Tauc plot and %Sn relative to Pb-Sn obtained from EDAX studies.

These values can be compared to the expected composition estimated via EDAX. Fig. 2b shows the results obtained by both approaches. It is worth to remark that our process results in films with compositions that are very close to the targeted ones, with insignificant batch-to-batch variations. The bandgap obtained for the different film thickness remains within the expected range, 1.2 and 1.4 eV, which confirms the compositional control achieved with the technique. These values are also close to previous reports on MA$_{0.9}$Cs$_{0.1}$Sn$_{0.25}$Pb$_{0.75}$I$_3$.[25]

The morphological, structural and optical characterization of the perovskite films indicate their suitability as absorbers in solar cells. The perovskite solar cells were prepared using a p-i-n configuration MoO$_3$/m-MTDATA/MA$_{0.9}$Cs$_{0.1}$Sn$_{0.25}$Pb$_{0.75}$I$_3$/C$_{60}$/BCP/Ag. m-MTDATA was used as its highest occupied molecular orbital (HOMO) aligns well with the expected perovskite energy levels, blocking electrons and allowing holes to pass.[25,32]

The current-voltage characteristics of representative devices under AM1.5G illumination are plotted in Fig. 3a, with their main averaged photovoltaic parameters represented in Fig. 4 and in Table 1. The current voltage curve reaches a power conversion efficiency value of 8.9% in forward measurement for devices based on a ~600 nm thick absorber. To understand the suitability of this thickness, it is important to analyze the main photovoltaic parameters of the devices. The short circuit current of the devices (J_{sc}) is enhanced as the perovskite thickness is increased from 200 nm to 600 nm (Fig. 3a), directly related to the absorbance shown in Fig. 2a. The external quantum efficiency (EQE) results (Fig. 3b) confirms this point. Devices based on thinner films show an EQE deficit at longer wavelengths, which is improved by increasing the film thickness up to 600 nm, in accordance with previous studies.[33] This can be explained by the lower absorption coefficient of Sn:Pb (0.25:0.75) vs Sn:Pb (0.5:0.5), which requires thicker films to absorb the less energetic photons but this ratio presents the bandgap we are searching for.[34] However, further increase of the perovskites thickness (650 and 700 nm) results in a reduction of the whole EQE response. Indeed, the trend with the film thickness in the shorter wavelengths is less clear, which can be due to problems related to the charge collection efficiency or to the parasitic absorption of unconverted metal halides compounds as suggested by the XRD analysis. As a result, the best performing devices were prepared with a perovskite film thickness of 600 nm, implying that by increasing the thickness some of the loses in the IR region could be avoided. The maximum theoretical J_{sc} for a bandgap of 1.3 eV is 35.8 mA/cm^2,[5] which indicates that further optimization could lead to higher currents.
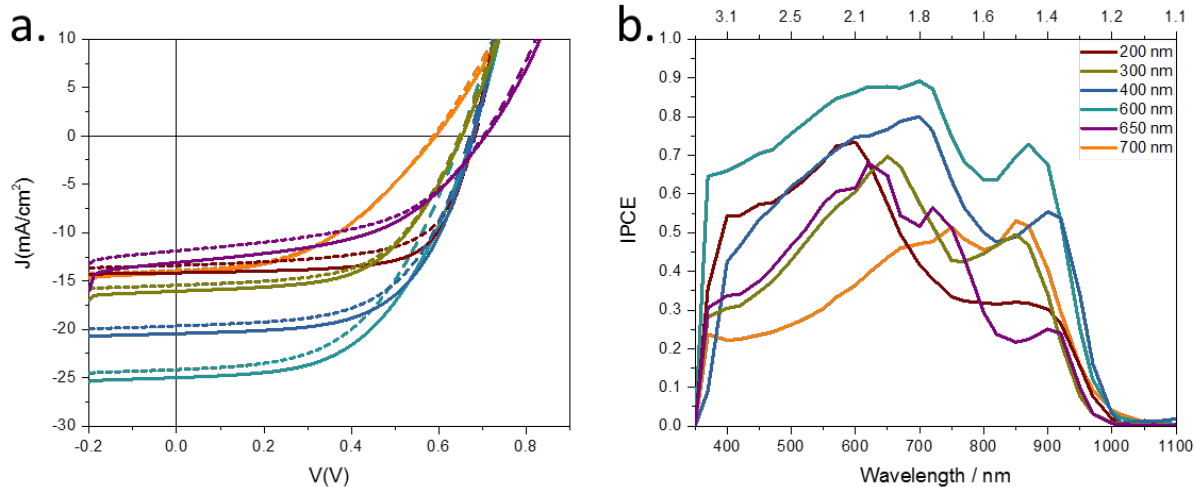

Fig. 3. (a) J-V measurements of solar cells with different MA$_{0.9}$Cs$_{0.1}$Sn$_{0.25}$Pb$_{0.75}$I$_3$ thicknesses under AM1.5G illumination. Dashed lines represent backward measurements and solid lines represent forward measurements (from negative to positive potential). (b) EQE of the representative devices.

In addition to the J_{sc} increase, a fill factor (FF) decrease and is also correlated to the film thickness, as displayed in Fig. 3a and 4a. FF reductions are usually originated by an impaired charge transport or by higher charge carrier recombination. The open circuit potential (V_{oc}) values do not show significant differences between 200nm and 400nm thick devices (Fig. 4c), which indicates similar recombination for the three groups and hints towards charge transport deficits as the origin of the FF reduction. This is in line with the resistances obtained for dark current voltage at high injection potential (>0.9 V) plotted in Fig. S6, which suggest that thicker films have larger series resistance.[35] The combination of all these parameters results in an optimal PCE for devices based on perovskite absorbers with thickness between 400 nm and 600 nm, as displayed in Fig 4d.
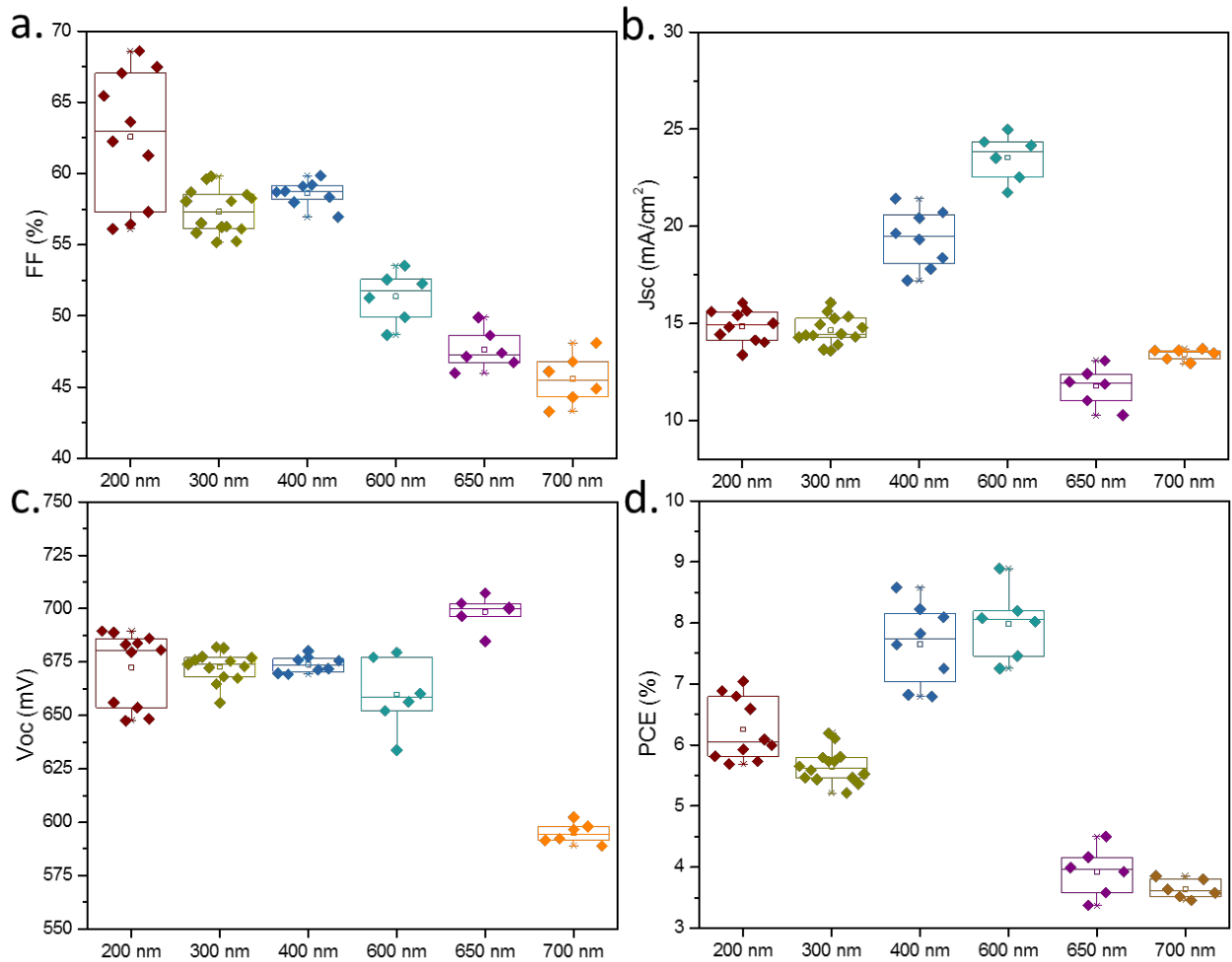
Fig. 4. Photovoltaic parameters of the devices with different perovskite thicknesses measured under AM1.5G illumination: (a)FF, (b) J_{sc} (c) V_{oc} and (d) PCE.

Table 1. Photovoltaic parameters under AM1.5G illumination measured for the representative solar cells of each thickness. Averaged values in brackets.

Thickness (nm)	FF (%)	J_{sc} (mA/cm^2)	V_{oc} (mV)	PCE (%)
200	62 (63)	14.0 (14.9)	686 (671)	6.0 (6.2)
300	60 (57)	15.3 (14.6)	677 (673)	6.2 (5.6)
400	59 (59)	20.4 (19.4)	680 (674)	8.2 (7.7)
600	53 (51)	25.0 (23.6)	677 (660)	8.9 (7.9)
650	49(48)	12.5(11.8)	704(699)	4.3(3.9)
700	47 (46)	13.7 (13.4)	592 (595)	3.8 (3.6)

V_{oc} decreases when perovskite films thicker than 400 nm are used. In order to understand this decrease, we measure impedance spectroscopy of 400 nm, 600 nm and 700 nm samples under 0.5 sun illumination. Generally, the impedance spectrum consisted of two features, a high frequency and a lower frequency one (see Fig. S7a), similar to previous reports on Pb-based perovskite solar cells.[36] Both arcs include information on the recombination,[37] which can be fitted with the equivalent circuit in Fig. S7b as discussed elsewhere.[38] In detail, the parameters of the circuit include an ohmic series resistance (R_s) which accounts for the TCO and cables transport with negligible capacitance; a low frequency capacitance (C_{dr}) whose origin is currently under discussion;[39–42] a device geometrical capacitance (C_g) and a resistance which includes the recombination resistance effects (R_{rec}) and a third of the transport resistance (displayed as R_{tr}), combined as ($R_{rec} + R_{tr}$). The $R_{rec}+R_{tr}$ values, represented in Fig. 5, clearly follow the trend of the V_{oc}, suggesting the they are dominated by the recombination processes. More interestingly, the volumetric normalization of this resistance reduces notably the differences among the samples (Fig. S7c). Altogether, the results suggest a bulk-dominant recombination process, in line with the V_{oc} and FF evolution.[23–25]
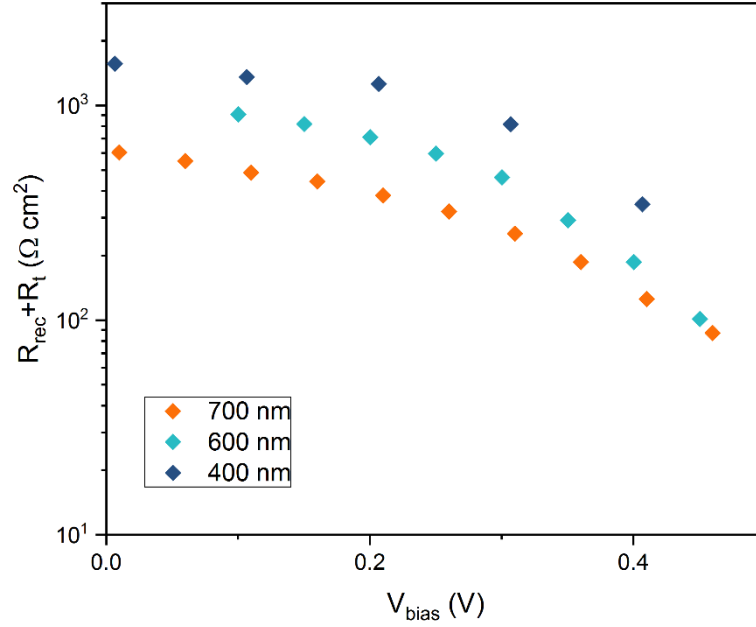
Fig. 5. Combination of recombination and transport resistances extracted from the impedance spectra of devices with different perovskite thicknesses measured under 0.5 sun illumination.

This trend is in good agreement with the V_{oc} evolution with the light intensity for the 600 nm absorber device, represented in Fig. S8. These measurements result in an ideality factor of ~2, which indicates trap-mediated recombination as the main loss process associated to these devices, in line with a bulk-dominated recombination. Vacuum-deposited Sn-Pb perovskites reported here present significantly smaller grain domains than their solution-processed counterparts.[34] Although the smaller grain size does not seem to have a significatively detrimental effect in vacuum-deposited lead perovskites, its combination with the Sn^{2+} oxidation could explain this bulk-recombination enhancement. Altogether, these results imply the need to reduce the bulk recombination in the films in order to be able to absorb longer wavelengths yet circumventing the losses associated to thicker absorbers.

CONCLUSIONS

We present a vacuum-deposition route to fabricate tin-lead perovskites for photovoltaic applications with reproducible results. Power conversion efficiencies of 8.9% was achieved with an optimization of the material composition and film thickness. The characterization of relevant material properties allowed to assess the suitability of this kind of perovskites for photovoltaic applications, correlating to the film operation in working devices. The limiting factors of the photovoltaic performance are analyzed by impedance spectroscopy, which indicates significant bulk recombination in devices with thicker perovskite absorbers.

Supporting Information. Schematic representation of evaporation chamber, XRD measurements, optical absorbance, photovoltaic characterization, current-voltage characteristics in dark conditions, impedance spectroscopy data, ideality factor estimation.

ACKNOWLEDGEMENT

BIBLIOGRAPHY

(1)   Kojima, A.; Teshima, K.; Miyasaka, T.; Shirai, Y.; Miyasaka, T. Novel Photoelectrochemical Cell with Mesoscopic Electrodes Sensitized by Lead-Halide Compounds (2). In *210th ECS Meeting*; **2006**.

(2)   Jiang, Q.; Zhao, Y.; Zhang, X.; Yang, X.; Chen, Y.; Chu, Z.; Ye, Q.; Li, X.; Yin, Z.; You, J. Surface Passivation of Perovskite Film for Efficient Solar Cells. *Nat. Photonics* **2019**, *13*, 460–466.

(3)   NREL https://www.nrel.gov/pv/cell-efficiency.html, **2019**.

(4)   Jeon, N. J.; Na, H.; Jung, E. H.; Yang, T. Y.; Lee, Y. G.; Kim, G.; Shin, H. W.; Il Seok, S.; Lee, J.; Seo, J. A Fluorene-Terminated Hole-Transporting Material for Highly Efficient and Stable Perovskite Solar Cells. *Nat. Energy* **2018**, *3* (8), 682–689.

(5)   Rühle, S. Tabulated Values of the Shockley-Queisser Limit for Single Junction Solar Cells. *Sol. Energy* **2016**, *130*, 139–147.

(6)   Chen, B.; Zheng, X.; Bai, Y.; Padture, N. P.; Huang, J. Progress in Tandem Solar Cells Based on Hybrid Organic–Inorganic Perovskites. *Adv. Energy Mater.* **2017**, *7* (14), 1602400.

(7)   Noel, N. K.; Stranks, S. D.; Abate, A.; Wehrenfennig, C.; Guarnera, S.; Haghighirad, A. A.; Sadhanala, A.; Eperon, G. E.; Pathak, S. K.; Johnston, M. B.; Petrozza, A; Herz, L. M., Snaith, H. J. Lead-Free Organic-Inorganic Tin Halide Perovskites for Photovoltaic Applications. *Energy Environ. Sci.* **2014**, *7* (9), 3061–3068.

(8)   Im, J.; Stoumpos, C. C.; Jin, H.; Freeman, A. J.; Kanatzidis, M. G. Antagonism between Spin-Orbit Coupling and Steric Effects Causes Anomalous Band Gap Evolution in the Perovskite Photovoltaic Materials CH3NH3Sn1-XPbxI3. *J. Phys. Chem. Lett.* **2015**, *6* (17), 3503–3509.

(9)   Gupta, S.; Cahen, D.; Hodes, G. How SnF2 Impacts the Material Properties of Lead-Free Tin Perovskites. *J. Phys. Chem. C* **2018**, *122* (25), 13926–13936.

(10)   Hao, F.; Stoumpos, C. C.; Chang, R. P. H.; Kanatzidis, M. G. Anomalous Band Gap Behavior in Mixed Sn and Pb Perovskites Enables Broadening of Absorption Spectrum in Solar Cells. *J. Am. Chem. Soc.* **2014**, *136* (22), 8094–8099.

(11)   Eperon, G. E.; Leijtens, T.; Bush, K. A.; Prasanna, R.; Green, T.; Wang, J. T. W.; McMeekin, D. P.; Volonakis, G.; Milot, R. L.; May, R.; Palmstrom, A; Slotcavage, D. J.; Belisle, R. A.; Patel, J. B.; Parrott, E. S.; Sutton, R. J.; Ma, W.; Moghadam, F.; Conings, B.; Babayigit, A.; Boyen, H. G.; Bent, S.; Giustino, F.; Herz, L. M.; Johnston, M. B.; McGehee, M. D.; Snaith, H. J. Perovskite-Perovskite Tandem Photovoltaics with Optimized Band Gaps. *Science (80-.).* **2016**, *354* (6314), 861–865.

(12)   Ogomi, Y.; Morita, A.; Tsukamoto, S.; Saitho, T.; Fujikawa, N.; Shen, Q.; Toyoda, T.; Yoshino, K.; Pandey, S. S.; Hayase, S. CH3 NH3 Snx Pb(1-x) I3 Perovskite Solar Cells Covering up to 1060 Nm. *J. Phys. Chem. Lett.* **2014**, *5*, 1004–1011.

(13)   Chen, M.; Ju, M. G.; Garces, H. F.; Carl, A. D.; Ono, L. K.; Hawash, Z.; Zhang, Y.; Shen, T.; Qi, Y.; Grimm, R. L.; Pacifici, D.; Zeng, X. C.; Zhou, Y.; Padture, N. P. Highly Stable and Efficient All-Inorganic Lead-Free Perovskite Solar Cells with Native-Oxide Passivation. *Nat. Commun.* **2019**, *10* (1), 1–8.

(14)	Kapil, G.; Ripolles, T. S.; Hamada, K.; Ogomi, Y.; Bessho, T.; Kinoshita, T.; Chantana, J.; Yoshino, K.; Shen, Q.; Toyoda, T.; Minemoto, T.; Murakami, T. N.; Segawa, H.; Hayase, S. Highly Efficient 17.6% Tin-Lead Mixed Perovskite Solar Cells Realized through Spike Structure. *Nano Lett.* **2018**, *18* (6), 3600–3607.

(15)	Li, C.; Song, Z.; Zhao, D.; Xiao, C.; Subedi, B.; Shrestha, N.; Junda, M. M.; Wang, C.; Jiang, C. S.; Al-Jassim, M.; Ellingson, R. J.; Podraza, N. J.; Zhu, K.; Yan, Y. Reducing Saturation-Current Density to Realize High-Efficiency Low-Bandgap Mixed Tin–Lead Halide Perovskite Solar Cells. *Adv. Energy Mater.* **2019**, *9* (3), 1–9.

(16)	Tong, J.; Song, Z.; Kim, D. H.; Chen, X.; Chen, C.; Palmstrom, A. F.; Ndione, P. F.; Reese, M. O.; Dunfield, S. P.; Reid, O. G.; Liu, J.; Zhang, F.; Harvey, S. P.; Li, Z.; Christensen, S. T.; Teeter, G.; Zhao, D.; Al-Jassim, M. M.; van Hest, M. F. A. M.; Beard, M. C.; Shaheen, S. E.; Berry, J. J.; Yan, Y.; Zhu, K. Carrier Lifetimes of >1 Ms in Sn-Pb Perovskites Enable Efficient All-Perovskite Tandem Solar Cells. *Science (80-.).* **2019**, *364* (6439), 475–479.

(17)	Ávila, J.; Momblona, C.; Boix, P. P.; Sessolo, M.; Bolink, H. J. Vapor-Deposited Perovskites: The Route to High-Performance Solar Cell Production? *Joule* **2017**, *1* (3), 431–442.

(18)	Ávila, J.; Momblona, C.; Boix, P.; Sessolo, M.; Anaya, M.; Lozano, G.; Vandewal, K.; Míguez, H.; Bolink, H. J. High Voltage Vacuum-Deposited CH $_3$ NH $_3$ PbI $_3$ –CH $_3$ NH $_3$ PbI $_3$ Tandem Solar Cells. *Energy Environ. Sci.* **2018**, *11* (11), 3292–3297.

(19)	Momblona, C.; Gil-Escrig, L.; Bandiello, E.; Hutter, E. M.; Sessolo, M.; Lederer, K.; Blochwitz-Nimoth, J.; Bolink, H. J. Efficient Vacuum Deposited P-i-n and n-i-p Perovskite Solar Cells Employing Doped Charge Transport Layers. *Energy Environ. Sci.* **2016**, *9* (11), 3456–3463.

(20)	Gil-Escrig, L.; Momblona, C.; La-Placa, M. G.; Boix, P. P.; Sessolo, M.; Bolink, H. J. Vacuum Deposited Triple-Cation Mixed-Halide Perovskite Solar Cells. *Adv. Energy Mater.* **2018**, *8* (14), 1–6.

(21)	Igual-Muñoz, A. M.; Ávila, J.; Boix, P. P.; Bolink, H. J. FAPb 0.5 Sn 0.5 I 3 : A Narrow Bandgap Perovskite Synthesized through Evaporation Methods for Solar Cell Applications . *Sol. RRL* **2019**, *1900283*, 1–5.

(22)	Kumar, M. H.; Dharani, S.; Leong, W. L.; Boix, P. P.; Prabhakar, R. R.; Baikie, T.; Shi, C.; Ding, H.; Ramesh, R.; Asta, M.; Graetzel, M.; Mhaisalkar, S. G.; Mathews, N. Lead-Free Halide Perovskite Solar Cells with High Photocurrents Realized through Vacancy Modulation. *Adv. Mater.* **2014**, *26* (41), 7122–7127.

(23)	Ball, J.; Buizza, L.; Sansom, H.; Farrar, M.; Klug, M.; Borchert, J.; Patel, J. B.; Herz, L. M.; Johnston, M. B.; Snaith, H. J. Dual-Source Co-Evaporation of Low-Bandgap FA1-XCsxSn1-

YPbyI3 Perovskites for Photovoltaics. *ACS Energy Lett.* **2019**, 4, 2748-2756.

(24)   Zhu, Z.; Li, N.; Zhao, D.; Wang, L.; Jen, A. K. Y. Improved Efficiency and Stability of Pb/Sn Binary Perovskite Solar Cells Fabricated by Galvanic Displacement Reaction. *Adv. Energy Mater.* **2019**, *9* (7), 2–9.

(25)   Liu, X.; Yang, Z.; Chueh, C. C.; Rajagopal, A.; Williams, S. T.; Sun, Y.; Jen, A. K. Y. Improved Efficiency and Stability of Pb-Sn Binary Perovskite Solar Cells by Cs Substitution. *J. Mater. Chem. A* **2016**, *4* (46), 17939–17945.

(26)   Niu, G.; Li, W.; Li, J.; Liang, X.; Wang, L. Enhancement of Thermal Stability for Perovskite Solar Cells through Cesium Doping. *RSC Adv.* **2017**, *7* (28), 17473–17479.

(27)   Li, R.; Yi, C.; Ge, R.; Zou, W.; Cheng, L.; Wang, N.; Wang, J.; Huang, W. Room-Temperature Electroluminescence from Two-Dimensional Lead Halide Perovskites. *Appl. Phys. Lett.* **2016**, *109* (15).

(28)   Dänekamp, B.; Droseros, N.; Palazon, F.; Sessolo, M.; Banerji, N.; Bolink, H. J. Efficient Photo- and Electroluminescence by Trap States Passivation in Vacuum-Deposited Hybrid Perovskite Thin Films. *ACS Appl. Mater. Interfaces* **2018**, *10* (42), 36187–36193.

(29)   Song, Z.; Watthage, S. C.; Phillips, A. B.; Tompkins, B. L.; Ellingson, R. J.; Heben, M. J. Impact of Processing Temperature and Composition on the Formation of Methylammonium Lead Iodide Perovskites. *Chem. Mater.* **2015**, *27* (13), 4612–4619.

(30)   McMeekin, D. P.; Mahesh, S.; Noel, N. K.; Klug, M. T.; Lim, J. C.; Warby, J. H.; Ball, J. M.; Herz, L. M.; Johnston, M. B.; Snaith, H. J. Solution-Processed All-Perovskite Multi-Junction Solar Cells. *Joule* **2019**, *3* (2), 387–401.

(31)   Palazon, F.; Pérez-del-Rey, D.; Dänekamp, B.; Dreessen, C.; Sessolo, M.; Boix, P. P.; Bolink, H. J. Room-Temperature Cubic Phase Crystallization and High Stability of Vacuum-Deposited Methylammonium Lead Triiodide Thin Films for High-Efficiency Solar Cells. *Adv. Mater.* **2019**, *31* (39), 1–6.

(32)   Aonuma, M.; Oyamada, T.; Sasabe, H.; Miki, T.; Adachi, C. Material Design of Hole Transport Materials Capable of Thick-Film Formation in Organic Light Emitting Diodes. *Appl. Phys. Lett.* **2007**, *90* (18), 1–4.

(33)   Wang, K.; Liu, C.; Du, P.; Chen, L.; Zhu, J.; Karim, A.; Gong, X. Efficiencies of Perovskite Hybrid Solar Cells Influenced by Film Thickness and Morphology of CH 3 NH 3 PbI 3-x Cl x

Layer. *Org. Electron. physics, Mater. Appl.* **2015**, *21*, 19–26.

(34)   Yang, Z.; Rajagopal, A.; Jen, A. K. Y. Ideal Bandgap Organic–Inorganic Hybrid Perovskite Solar Cells. *Adv. Mater.* **2017**, *29* (47), 1704418.

(35)   Liu, D.; Gangishetty, M. K.; Kelly, T. L. Effect of $CH_3NH_3PbI_3$ Thickness on Device Efficiency in Planar Heterojunction Perovskite Solar Cells. *J. Mater. Chem. A* **2014**, *2* (46), 19873–19881.

(36)   Contreras-Bernal, L.; Ramos-Terrón, S.; Riquelme, A.; Boix, P. P.; Idígoras, J.; Mora-Seró, I.; Anta, J. A. Impedance Analysis of Perovskite Solar Cells: A Case Study. *J. Mater. Chem. A* **2019**, *7* (19), 12191–12200.

(37)   Zarazua, I.; Han, G.; Boix, P. P.; Mhaisalkar, S.; Fabregat-Santiago, F.; Mora-Seró, I.; Bisquert, J.; Garcia-Belmonte, G. Surface Recombination and Collection Efficiency in Perovskite Solar Cells from Impedance Analysis. *J. Phys. Chem. Lett.* **2016**, *7* (24), 5105–5113.

(38)   Yoo, S.-M.; Yoon, S. J.; Anta, J. A.; Lee, H. J.; Boix, P. P.; Mora-Seró, I. An Equivalent Circuit for Perovskite Solar Cell Bridging Sensitized to Thin Film Architectures. *Joule* **2019**, 1–15.

(39)   Zarazua, I.; Bisquert, J.; Garcia-Belmonte, G. Light-Induced Space-Charge Accumulation Zone as Photovoltaic Mechanism in Perovskite Solar Cells. *J. Phys. Chem. Lett.* **2016**, *7* (3), 525–528.

(40)   Contreras, L.; Idígoras, J.; Todinova, A.; Salado, M.; Kazim, S.; Ahmad, S.; Anta, J. A. Specific Cation Interactions as the Cause of Slow Dynamics and Hysteresis in Dye and Perovskite Solar Cells: A Small-Perturbation Study. *Phys. Chem. Chem. Phys.* **2016**, *18* (45), 31033–31042.

(41)   Ebadi, F.; Taghavinia, N.; Mohammadpour, R.; Hagfeldt, A.; Tress, W. Origin of Apparent Light-Enhanced and Negative Capacitance in Perovskite Solar Cells. *Nat. Commun.* **2019**, *10* (1), 1574.

(42)   Moia, D.; Gelmetti, I.; Calado, P.; Fisher, W.; Stringer, M.; Game, O.; Hu, Y.; Docampo, P.; Lidzey, D.; Palomares, Nelson, J.; Barnes, P. R.F. Ionic-to-Electronic Current Amplification in Hybrid Perovskite Solar Cells: Ionically Gated Transistor-Interface Circuit Model Explains Hysteresis and Impedance of Mixed Conducting Devices. *Energy Environ. Sci.* **2019**, *12* (4), 1296–1308.

(43)   Pockett, A.; Eperon, G. E.; Peltola, T.; Snaith, H. J.; Walker, A.; Peter, L. M.; Cameron, P. J. Characterization of Planar Lead Halide Perovskite Solar Cells by Impedance Spectroscopy, Open-Circuit Photovoltage Decay, and Intensity-Modulated Photovoltage/Photocurrent Spectroscopy. *J. Phys. Chem. C* **2015**, *119* (7), 3456–3465.

(44)   Jacobs, D. A.; Shen, H.; Pfeffer, F.; Peng, J.; White, T. P.; Beck, F. J.; Catchpole, K. R. The Two

Faces of Capacitance: New Interpretations for Electrical Impedance Measurements of Perovskite Solar Cells and Their Relation to Hysteresis. *J. Appl. Phys.* **2018**, *124* (22), 225702.

(45)   Pitarch-Tena, D.; Ngo, T. T.; Vallés-Pelarda, M.; Pauporté, T.; Mora-Seró, I. Impedance Spectroscopy Measurements in Perovskite Solar Cells: Device Stability and Noise Reduction. *ACS Energy Lett.* **2018**, *3* (4), 1044–1048.

Vacuum-Deposited Multication Tin-Lead Perovskite Solar Cells

Ana M. Igual-Muñoz[1], Aroa Castillo[1], Chris Dreessen[1], Pablo P. Boix*[2], and Henk J. Bolink*[1].

[1] Instituto de Ciencia Molecular, Universidad de Valencia, C/J. Beltran 2, 46980 Paterna, Spain.

[2] Institut de Ciència dels Materials, Universitat de València, C/ J. Beltran 2, 46980 Paterna, Spain.

*E-mail: Pablo.P.Boix@uv.es; henk.bolink@uv.es
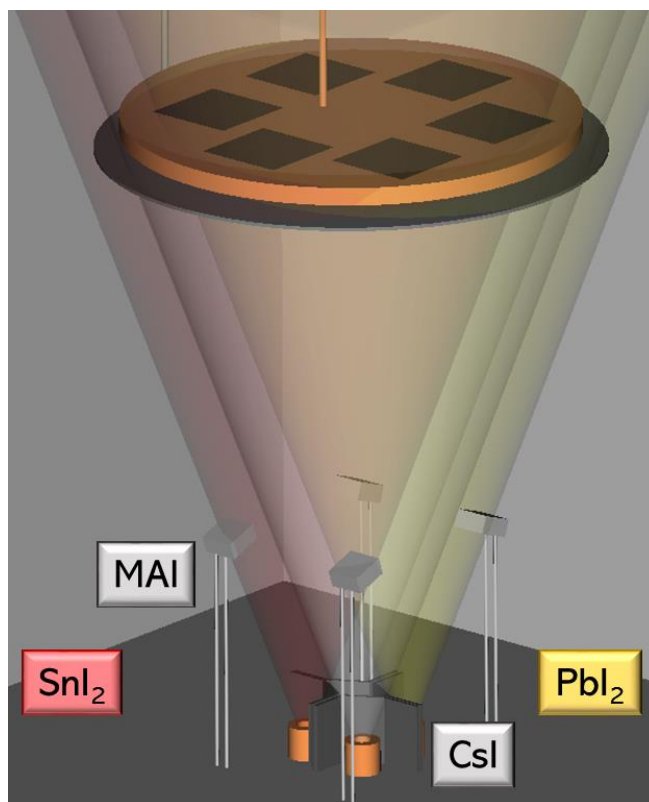
Figure S1. Scheme of the evaporator machine.
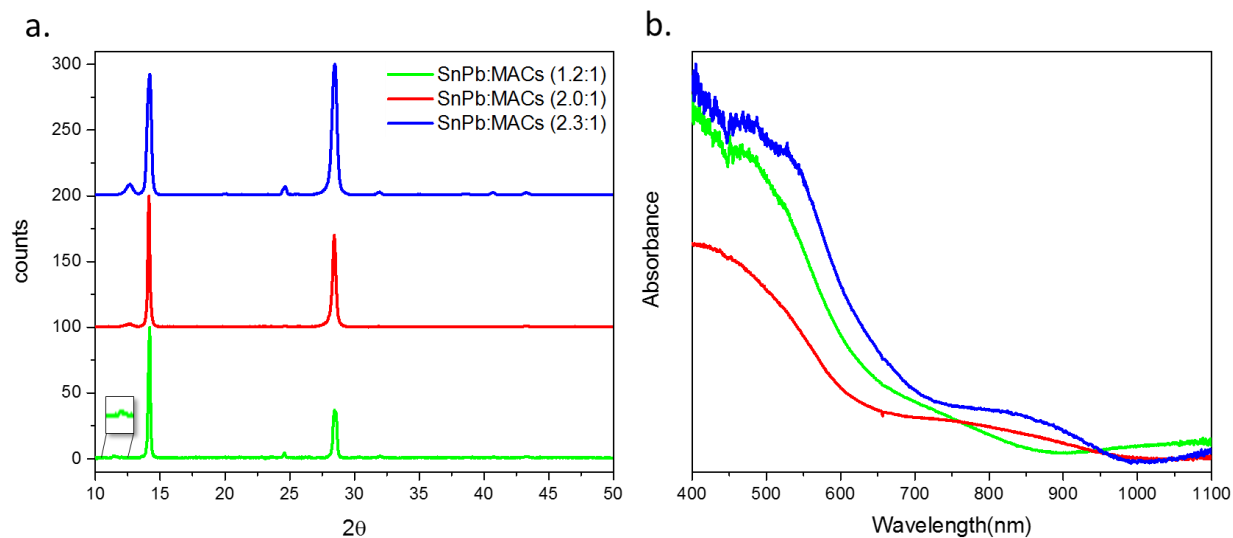
Fig. S2. a) XRD diagrams and b) absorbance of MA$_{0.9}$Cs$_{0.1}$Sn$_{0.25}$Pb$_{0.75}$I$_3$ films with different SnPb:MACs ratios.
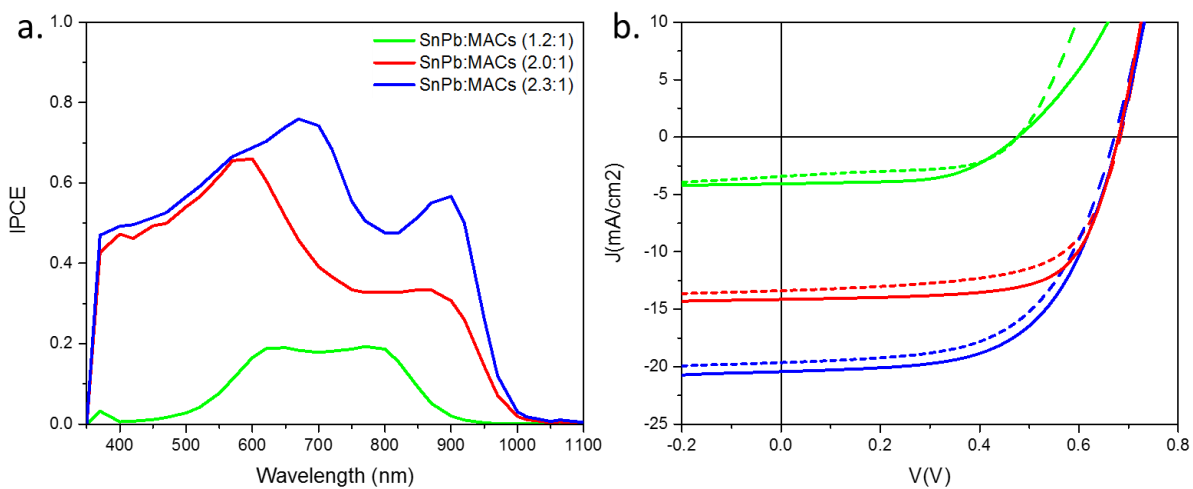
Fig. S3. (a) External quantum efficiency (EQE) and (b) JV measurement under light conditions for the solar cells made with different SnPb to MACs ratios. Dashed lines represent backward measurements and solid lines represent forward measurements (from negative to positive potential).

Table S1. Photovoltaic parameters under AM1.5G illumination measured for the solar cells represented in Fig. S2.

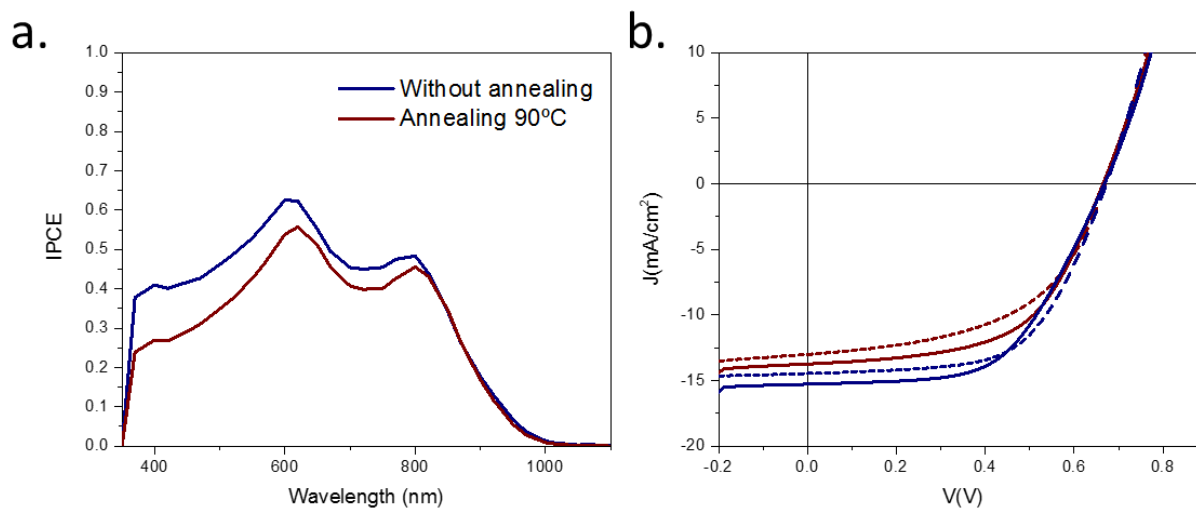| Ratio (SnPb:MACs)	FF (%)	J$_{sc}$ (mA/cm^2)	V$_{oc}$ (mV)	PCE (%)
1.2:1	57	3.7	477	1.0
2.0:1	66	13.7	681	6.1

| 2.3:1 | 59 | 21.1 | 673 | 8.4 |

Fig. S4. J-V characteristics measured in light conditions for cells prepared with and without thermal post-treatment of 90ºC for 5 minutes.
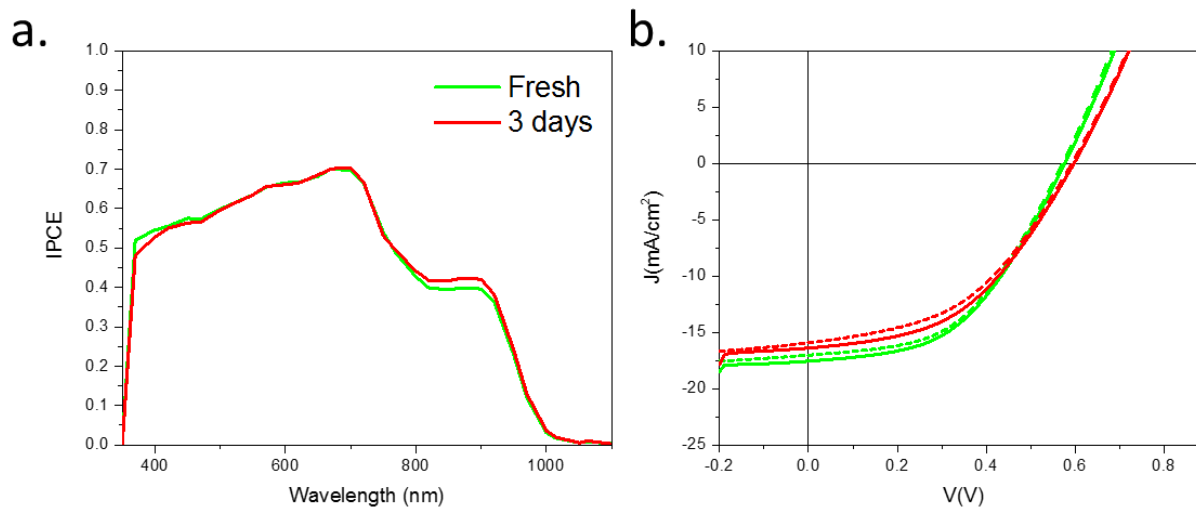

Fig. S5. J-V characteristics measured in light conditions for cells as prepared and after three days of storage in a glovebox containing N_2.
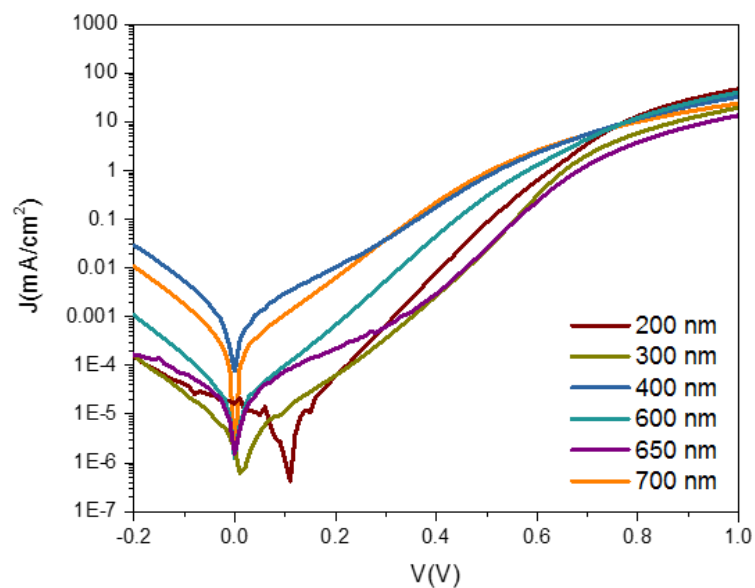
Fig. S6. J-V characteristics measured in dark conditions for the representative devices with different thicknesses.
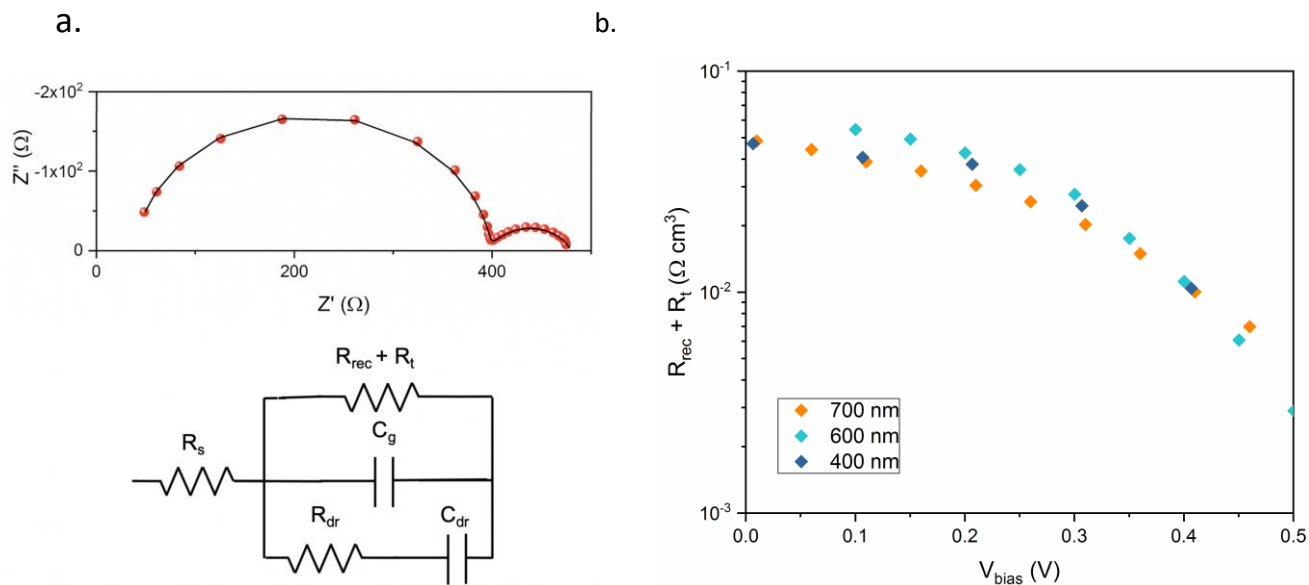
a.

b.

Fig. S7. (a) Representative Nyquist plot obtained for the 600 nm sample under 0.5 sun illumination. The dots correspond to the experimental data and the solid line is the fitting using the equivalent circuit in (b). (c) Volumetric normalization of $R_{rec} + R_t$.
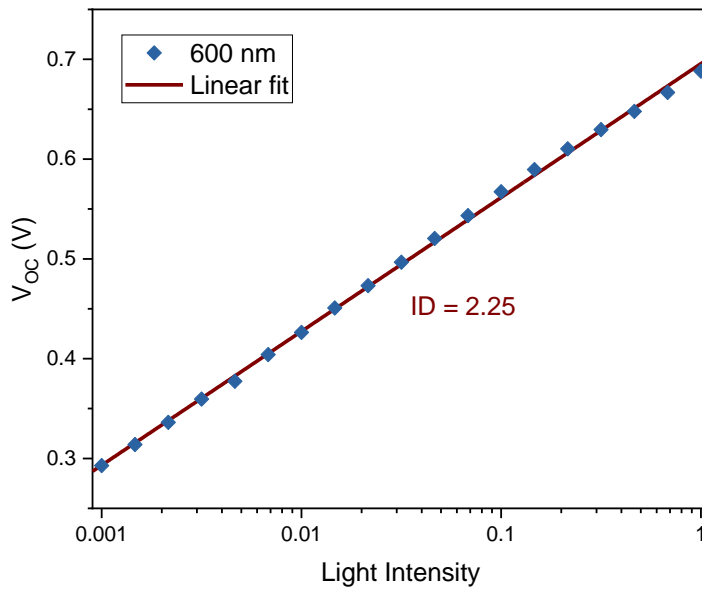
Figure S8. Voc vs the logarithm of light intensity for the determination of the ideality factor. Note that a light intensity of 1 corresponds to more than one sun illumination.